Buffer scheme for aero-performance deterioration caused by trains passing bilateral vertical noise barriers with crosswinds

E. Deng, Xin-Yuan Liu, Yi-Qing Ni, You-Wu Wang, Zheng-Wei Chen & Xu-Hui He

Published online: 06 Jan 2023.

Submit your article to this journal ↗

View related articles ↗

View Crossmark data ↗

Taylor & Francis
Taylor & Francis Group

Buffer scheme for aero-performance deterioration caused by trains passing bilateral vertical noise barriers with crosswinds

E. Deng[a,b], Xin-Yuan Liu[c], Yi-Qing Ni[a,b], You-Wu Wang[a,b], Zheng-Wei Chen[a,b] and Xu-Hui He[c,d]

[a]National Rail Transit Electrification and Automation Engineering Technology Research Center (Hong Kong Branch), Hong Kong, People's Republic of China; [b]Department of Civil and Environmental Engineering, The Hong Kong Polytechnic University, Hong Kong, People's Republic of China; [c]School of Civil Engineering, Central South University, Changsha, People's Republic of China; [d]National Engineering Research Center of High-speed Railway Construction Technology, Central South University, Changsha, People's Republic of China

ABSTRACT

Bilateral vertical noise barriers have been widely used along high-speed railway lines in coastal cities where typhoons are frequent. When a high-speed train (HST) enters (or exits) a noise barrier under strong crosswind conditions, its running safety will be more severely tested because of the instantaneous switching of aerodynamic environment. Installing a buffer structure at the end of the noise barrier is necessary to ensure the running safety of HSTs. In this study, two types of aerodynamic buffer structures (triangle and fence types) for the end of the noise barrier are proposed. The buffering effects of the two structures on the sudden change amplitude of the aerodynamic load of the carriage are compared by using an improved delayed detached eddy simulation method. The difference in the influence of the two buffer structures on the aerodynamic responses of the carriage is discussed by using a wind–train–bridge coupling dynamic response calculation method. The buffer mechanisms of the two structures are revealed in terms of the flow field. Results show that the buffering effect of fence type is superior triangle type, and the buffer length of 4 L is the most reasonable.

1. Introduction

At present, high-speed rail networks in China's coastal cities have been completed. Coastal areas, especially in southeast China, are subject to periodic extreme weather conditions such as strong winds and typhoons (He et al., 2022). The safety of a high-speed train (HST) is seriously threatened when it encounters strong winds during its operation (Gao et al., 2021; Liao et al., 2023). The noise generated by HSTs affects the quality of life of urban residents when they pass through the centre of a city where residents gather (Li et al., 2022). Accordingly, a noise barrier is covered along this section. As shown in Figure 1, the most common type is bilateral vertical noise barrier (Xiong et al., 2020). This type of noise barrier installation scheme covers only the railway segment with noise reduction requirement to save construction cost. When a HST enters (or exits) a noise barrier under strong crosswind conditions, its running safety will be more severely tested because of the instantaneous switching of aerodynamic environment. Installing a buffer structure at the

end of the noise barrier is necessary to ensure the running safety of HSTs.

Some researchers have conducted a series of studies on the aerodynamic effects caused by the relative motion between the train and the noise barrier. For the enclosed noise barrier, Jing et al. (2022) studied the longitudinal transmission law of aerodynamic pressure waves and the attenuation characteristics of peak pressure inside a fully-enclosed noise barrier when a HST passes through based on computational fluid dynamics (CFD) simulation. Similarly, Zheng et al. (2022) conducted a series of field tests on the train-induced aerodynamic pressure wave propagation law near the entrance of the fully-enclosed noise barrier and revealed the generation mechanism of inlet compression wave from the perspective of influencing factors, such as train marshalling length and running speed. For the vertical noise barrier, Soper et al. (2019) performed a series of field tests and found that the train type has a remarkable impact on the aerodynamic pressure exerted on a unilateral vertical noise barrier. Xiong

Figure 1. Typical bilateral vertical noise barrier.

et al. (2020) focused on the dominant frequency characteristics of the aerodynamic pressure impact of HSTs on vertical noise barriers based on field tests. Qiu et al. (2022) further studied the aerodynamic pressure pulse characteristics of the vertical noise barrier beside the track when two trains meet through CFD dynamic model simulation. The above studies researches mainly focus on the characteristics of train-induced aerodynamic pressure on the noise barrier itself and ignore the influence of crosswind.

Some researchers have observed noticed that the aerodynamic performance of vehicles deteriorates remarkably when they pass the trackside facilities with abrupt boundaries under crosswind conditions. For the road vehicles, Zhang et al. (2020) and Wang et al. (2021) established a coupling model of aerodynamic dynamics and multi-body dynamics to reveal the aerodynamic characteristics of a sedan when it exits the tunnel and passes through the bridge pylon area under action of crosswind. Chen et al. (2019) revealed that the yaw stability of a truck is remarkably worse when it drives from a bridge to a tunnel under the action of strong crosswinds based on the driving simulator. Compared with road vehicles, trains have a much larger slenderness ratio. In particular, HSTs run several times faster than road vehicles. Liu et al. (2018) and Chen et al. (2022) conducted a series of CFD simulation studies on the aerodynamic characteristics of a HST passing through a transition from ground to cutting in a windy area and described the yaw motion of the train body over time during the sudden change in

the flow field in this section. Zhou et al. (2021) analysed the variation of flow structure around the HST running on a bridge–tunnel section with and without crosswinds by using CFD and revealed the influence mechanism of rapid infrastructure switching on the aerodynamic characteristics of the train. The installation of windproof facilities is often necessary to ensure the running safety of HSTs in crosswind environment. For the deterioration of aerodynamic performance at the end of a windproof structure, Zhang, Thurow, et al (2018) derived the calculation formula of sudden wind load acting on the train body when the train enters or exits the wind barrier and analysed the influence of sudden wind load on the running safety. On this basis, Yang et al. (2019) and Deng et al. (2019) systematically evaluated the traffic safety deterioration degree of HSTs at the end of windproof facilities (anti-wind open-cut tunnel and windbreak wall) in windy area. However, mitigation measures are still lacking for the above-mentioned train running safety hazards.

Current studies on the aerodynamic buffer structures of high-speed railway infrastructure are mainly limited to alleviating pressure wave gradient at the tunnel entrance and micropressure wave at the tunnel exit without considering the crosswind. In the early stage, Winslow and Howe (2005) designed two types of aerodynamic buffer structure of a tunnel portal, namely, flared type and stepped-portal type, to alleviate the initial compression wave generated when a HST enters a tunnel. Similarly, Wang et al. (2022) designed a variable cross-section

tunnel entrance to improve passenger pressure comfort when trains intersect in the tunnel. Subsequently, the equal-transect oblique tunnel portal structure has been gradually popularised and applied to high-speed railway tunnels. Zhang, Xia, et al. (2018) confirmed the effectiveness of a hat oblique tunnel portal structure to alleviate the pressure gradient and micropressure wave, and revealed its buffering mechanism by using CFD simulation and moving model tests. For the suppression of the micropressure wave in high-speed railway tunnel, Miyachi and Fukuda (2021) found that the gradient of compression pressure wave can be effectively reduced by optimising the hole layout on the tunnel entrance hoods based on moving model test. From the perspective of bionics, Kim et al. (2021) designed an entrance hood with air slits attached on each side to alleviate the micropressure wave at the exit of the tunnel, inspired by shark gill respiration. Unfortunately, few studies are reported on the buffer measures for sudden aerodynamic loads of trains under crosswind conditions.

Two types of aerodynamic buffer structures (triangle and fence types) are proposed for the end of the noise barrier in this study to address the aerodynamic performance deterioration of trains passing through the end of the bilateral vertical noise barrier under crosswind. The buffering effects of the two structures on the sudden change amplitude of the aerodynamic load of the carriage are compared by using an improved delayed detached eddy simulation (IDDES) method. The difference in the influence of the two buffer structures on the aerodynamic response indexes of the carriage is discussed by using a wind–train–bridge coupling dynamic response calculation method, and the sensitivity analysis of the design parameters (longitudinal length of buffer structure) is conducted. The buffer mechanisms of the two structures are revealed in terms of the flow field, and the optimal buffer scheme is determined.

2. Methodology

2.1. IDDES method

2.1.1. Turbulence model

The detached eddy simulation (DES) method combines the advantages of Reynolds-averaged Navier–Stokes (RANS) and large eddy simulation (LES) methods. The delayed DES (DDES) method can prevent the vortex separation caused by the model stress loss and improper mesh refinement. The improved DDES (IDDES) method can solve the problem of logarithmic region mismatch well (Dong et al., 2022). Thus, the IDDES scheme is used in the CFD simulation in this study. The shear stress transport k–ω two-equation model (SST k–ω) is used to

simulate the flow field near the train surface (Li et al., 2021). The length scale of the IDDES method can be estimated as follows.

$$l_{hyb} = f_{hyb}(1 + f_e)l_{RANS} + (1 - f_{hyb})l_{LES}, \tag{1}$$

$$f_{hyb} = \max \left\{ \tanh \left[\left(20 \frac{\nu_t}{\kappa^2 d_w^2 \sqrt{0.5(\mathbf{S}^2 + \Omega^2)}} \right)^3 \right], f_{step} \right\}, \tag{2}$$

where f_{hyb} is a mixed function; f_e is a boost function that is designed to prevent excessive reduction of RANS Reynolds stress; l_{RANS} and l_{LES} represent the scales of RANS and LES regions, respectively; d_w is the distance from the wall; ν_t is the eddy viscosity; κ is the Von Karman constant; $\mathbf{S}$ and Ω are the stain rate and rotation rate tensors normalised by the turbulence time scale, respectively; f_{step} is a function that provides a quick switch from RANS to LES at the depth of the boundary layer, which can only be activated under the wall-modelled LES mode.

2.1.2. Buffer structural parameters and geometric model

Two types of buffer structures for the end of the bilateral vertical noise barrier, namely, triangle and fence types, are discussed in this study (Figure 2). The buffer structures corresponding to the noise barrier are bilateral. For the triangle type (TRI), three length parameters, namely, 2, 4 and 6 L (L is the length of the head carriage of HST, 25 m) are considered. For the fence type, the fence with gradient porosity along the longitudinal direction (FGPL) is assembled from several unit plates, each of length L. The porosity of the unit plate decreases linearly from the outside to the inside along the longitudinal direction. Three length parameters corresponding to the TRI are obtained by adjusting the number of unit plates, as shown in Figure 2(b).

Figure 3 shows the geometric parameters and boundary conditions of the CFD model calculation domain in this study. The HST model is CRH380B. It adopts the marshalling form of three carriages (head, middle and tail), the width of the carriage cross section is W (3.26 m), and the height is H (3.89 m). The distance between the initial position of the HST noise tip and the inlet end of the noise barrier is 7.6 L. The origin of the coordinate system of the global model is located at the initial position of the gravity centre of head carriage. The bridge is modelled with reference to the 32 m simply supported box girder made of prestressed concrete. The height of the noise barrier is 1.3 H, the thickness is 0.5 W, and the length is 5.8 L.

The atmospheric boundary of the model was constructed with a semicylindrical wall with a diameter of
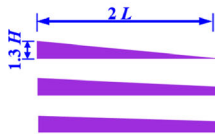
Figure 2. Parameters of the buffer structures: (a) triangle type and (b) fence type.
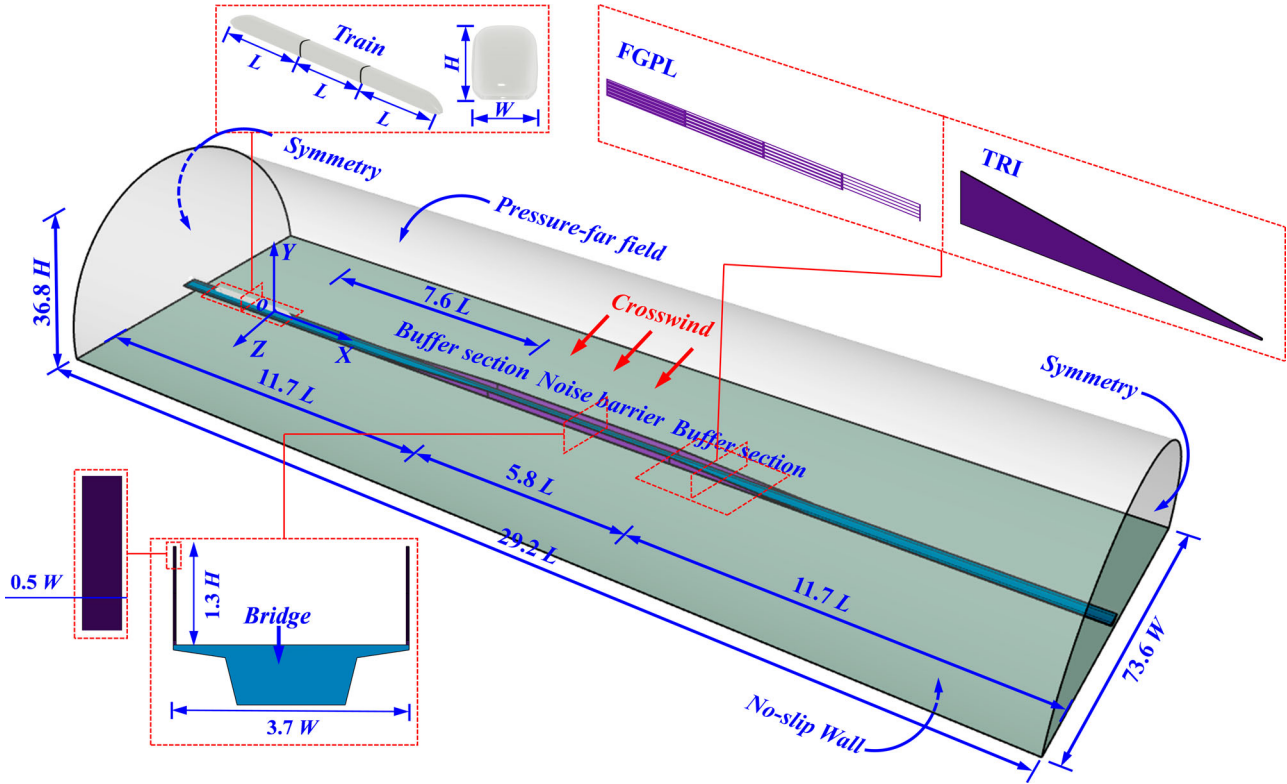

Figure 3. Geometry and boundary conditions.

73.6 W, and the corresponding boundary condition was set as pressure-far field. A constant crosswind condition with a velocity of 30 m/s can be obtained by setting a Mach number of 0.0864 along the positive Z direction on the pressure-far field boundary. No-slip wall is applied to the outer walls of the train, bridge, noise barrier, buffer structures and the ground. The setting of the remaining boundary conditions is shown in Figure 3.

2.1.3. Grid details and solution strategies

As shown in Figure 4, the computation is divided into two regions, the static grid region (B) and the moving grid region (A). Region A is further divided into three segments, namely, A_0, A_1 and A_2. Regions A_1 and B are discretised by using polyhexcore grids, and regions A_0 and A_2 are discretised by using structured grids. The dynamic layering method is used to realise the train movement. The train runs in the positive X direction at a constant speed of 250 km/h and is controlled by a user-defined function programme. The average size of the grids on the train surface and noise barrier surface is about 0.02 and

0.05 m, respectively. The grid size of the first refinement region covering the bridge and noise barrier is limited to within 0.05 m. The boundary layer parameters of the train, bridge and barrier are shown in the zoom window of Figure 4. The total number of elements in the base line (BL, the bilateral vertical noise barrier without buffer structure) model is about 35 million.

The grid model is imported into Fluent and solved by using transient mode and second-order implicit scheme. The number of iterations per time step is 20, and the time step is 0.001 s. The computing equipment is a supercomputer with a 6-node, 144-core processor, and the computing time of each case is about 2 weeks.

2.2. Wind–train–bridge–noise barrier coupling model

A simplified calculation model of wind–train–bridge–noise barrier coupling dynamic response is established by considering the aerodynamic loads on the train, bridge and noise barrier simultaneously. This model is used to
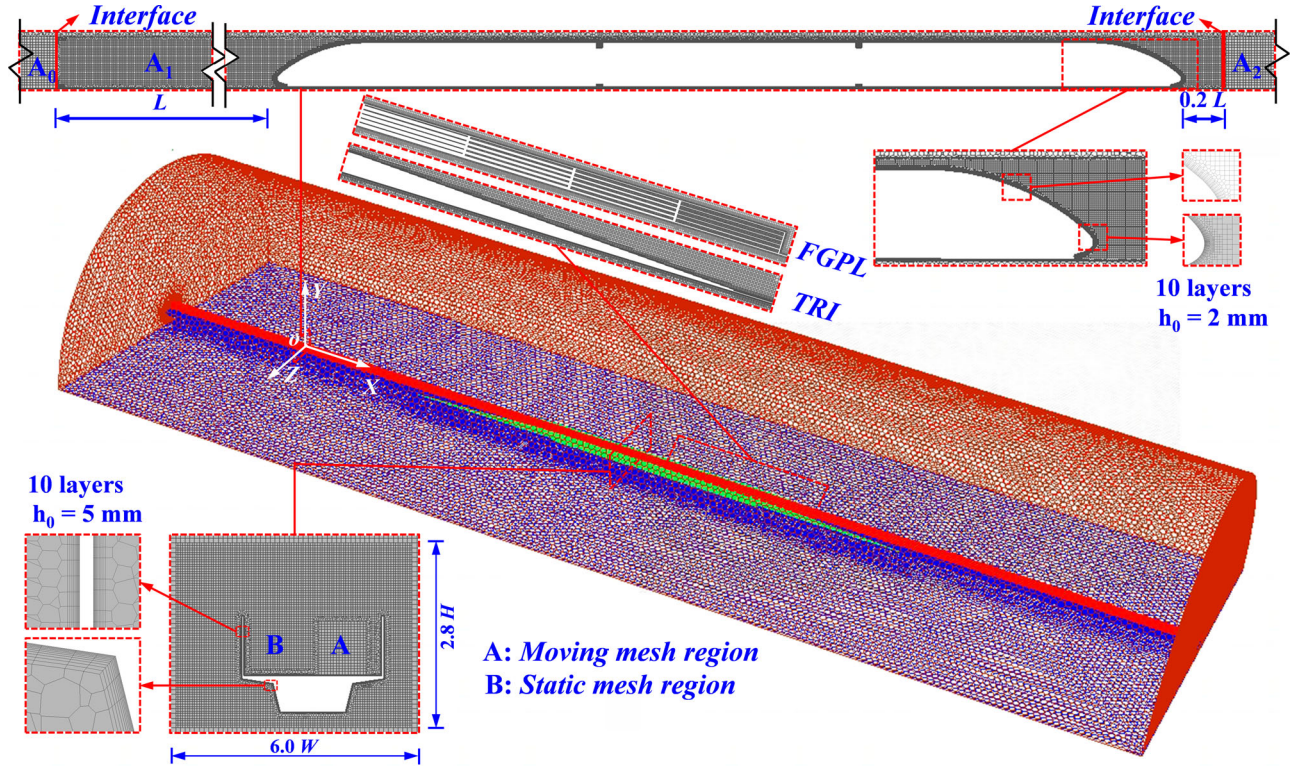
Figure 4. Grid model.

evaluate the buffering effect of the buffer structure on the dynamic response of the vehicle system. A schematic of the coupling system is shown in Figure 5, and the equation of motion is as follows.

$$\begin{cases} \mathbf{M}_T\ddot{\mathbf{X}}_T + \mathbf{C}_T\dot{\mathbf{X}}_T + \mathbf{K}_T\mathbf{X}_T = \mathbf{F}_T \\ \mathbf{M}_B\ddot{\mathbf{X}}_B + \mathbf{C}_B\dot{\mathbf{X}}_B + \mathbf{K}_B\mathbf{X}_B = \mathbf{F}_B \end{cases}, \quad (3)$$

$$\mathbf{F}_T = \begin{bmatrix} F_{tc} & F_{tb1} & F_{tb2} & F_{tw1} & F_{tw2} & F_{tw3} & F_{tw4} \end{bmatrix}^T, \quad (4)$$

$$\begin{cases} F_{tc} = \begin{bmatrix} F_y^t - G_c & F_z^t & M_x^t & M_y^t & M_z^t \end{bmatrix}^T \\ F_{tbi} = \begin{bmatrix} -G_{bi} & 0 & 0 & 0 & 0 \end{bmatrix}^T (i = 1, 2) \\ F_{twj} = \begin{bmatrix} F_{yj}^{irr} - G_{wj} & F_{zj}^{irr} & M_{xj}^{irr} & M_{yj}^{irr} & 0 \end{bmatrix}^T, \\ (j = 1, 2, 3, 4) \end{cases}$$

$$(5)$$

$$\mathbf{F}_B = \begin{bmatrix} F_y^b - G_B - F_y^{irr} & F_z^b + F_z^{irr} & M_x^b + M_x^{irr} & 0 & 0 \end{bmatrix}^T, \quad (6)$$

where **M**, **C** and **K** represent the mass, damping and stiffness matrices, respectively, subscript T refers to the train subsystem (single carriage), and B refers to the bridge–noise barrier subsystem; $\ddot{\mathbf{X}}$, $\dot{\mathbf{X}}$ and $\mathbf{X}$ represent the acceleration, velocity and displacement matrices, respectively; $\mathbf{F}$ represents the external excitation load on the corresponding subsystem; G_c, G_b and G_w represent the gravity of carriage body, bogie and wheelset,

respectively; F_y^t, F_z^t, M_x^t, M_y^t and M_z^t represent the aerodynamic lift and side forces, rolling, yawing and pitching moments on the carriage body, respectively (Yang et al., 2019); F_y^{irr}, F_z^{irr} and M_x^{irr} represent the excitation generated by the track irregularity at the corresponding degrees of freedom, respectively; G_B represents the gravity of a single-span 32 m box girder; F_y^b, F_z^b and M_x^b represent the aerodynamic lift and side forces and rolling moment on the single-span box girder, respectively.

In the present coupling model, five degrees of freedom, namely, Y_{tc}, Z_{tc}, ϕ_{tc}, ψ_{tc} and β_{tc}, are considered for the carriage body. Only three degrees of freedom, namely Y_b, Z_b and ϕ_b, are considered for the single-span box girder. On the basis Hertz nonlinear elastic contact theory, a 3D space trace method is used to solve the geometry contact relationship between the wheel and rail. The track irregularity spectrum is based on China high-speed railway ballastless track spectrum (TB/T 3352-2014, 2014). The specific values of the corresponding parameters in Equations (3)–(6) and the solution details are given in (Deng et al., 2019).

2.3. Verification

2.3.1. Grid independence verification
The mesh size is related to the computational accuracy and computational efficiency of the numerical model.
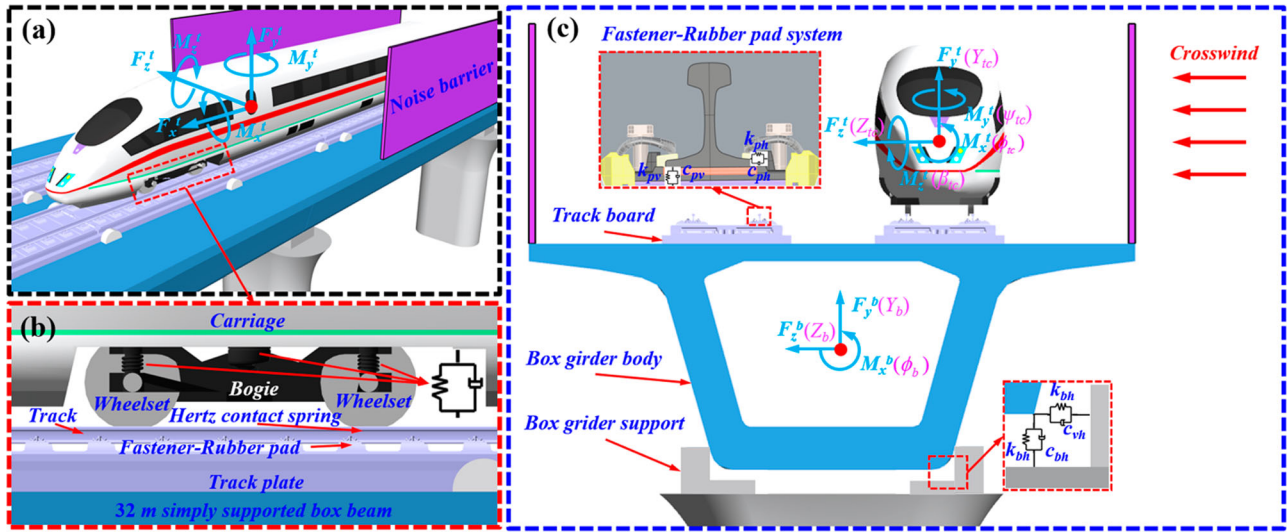
Figure 5. Schematic of the wind–train–bridge–noise barrier coupling system: (a) Three-dimensional view; (b) wheel–rail contact model and (c) cross section view.
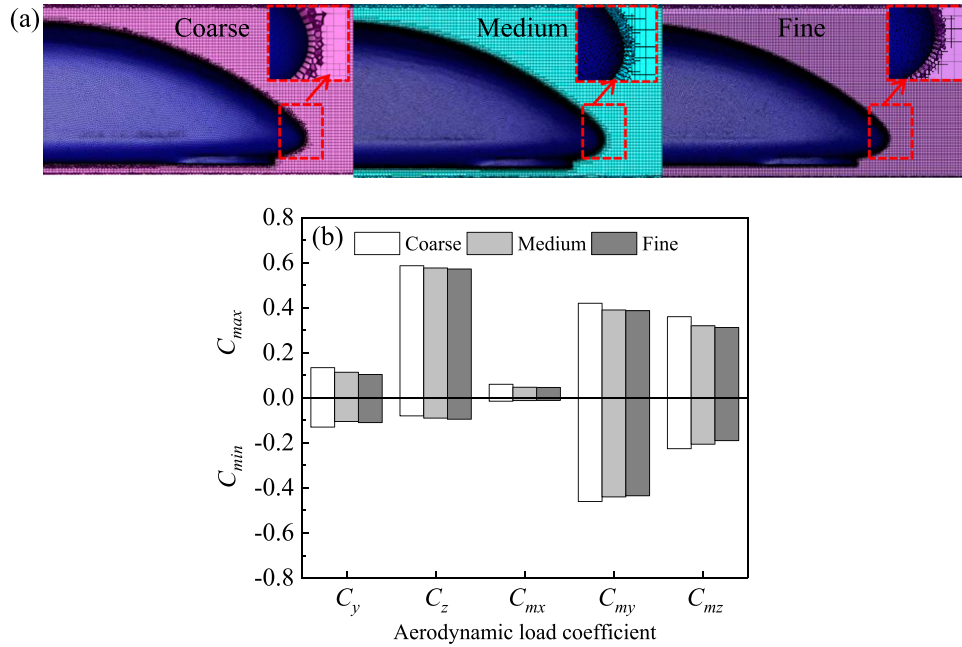

Figure 6. Verification of mesh independence: (a) train meshes with different resolutions; (b) aerodynamic load coefficient of the head carriage.

Figure 6 shows the comparison of the five peak coefficients (i.e. lift force coefficient C_y, side force coefficient C_z, rolling moment coefficient C_{mx}, yawing moment coefficient C_{my} and pitching moment coefficient C_{mz}, and the dimensionless method is based on BS EN, 2006 and Deng et al., 2019) of the head carriage of the numerical model with different mesh quantities when the train enters the noise barrier, where the number of boundary layers and the height of the first boundary layer are kept unchanged. The grid volumes corresponding to the three grid sizes are about 25 million (coarse), 35 million (middle) and 40 million (fine). From the analysis of Figure 6(b), the positive and negative peaks of each aerodynamic load corresponding to the coarse mesh are larger than the corresponding values of the medium and fine meshes. For example, the positive lift peak value of the coarse mesh is 17.6% higher than the corresponding value of the medium mesh, and this remarkable difference is reflected in the yawing moment and pitching moment coefficients. The positive peak lift of the medium mesh is only 4.2% higher than that of the fine mesh, and the difference between the positive and negative peak coefficients of the medium and fine meshes is less than 10% in the other four aerodynamic load coefficients. The
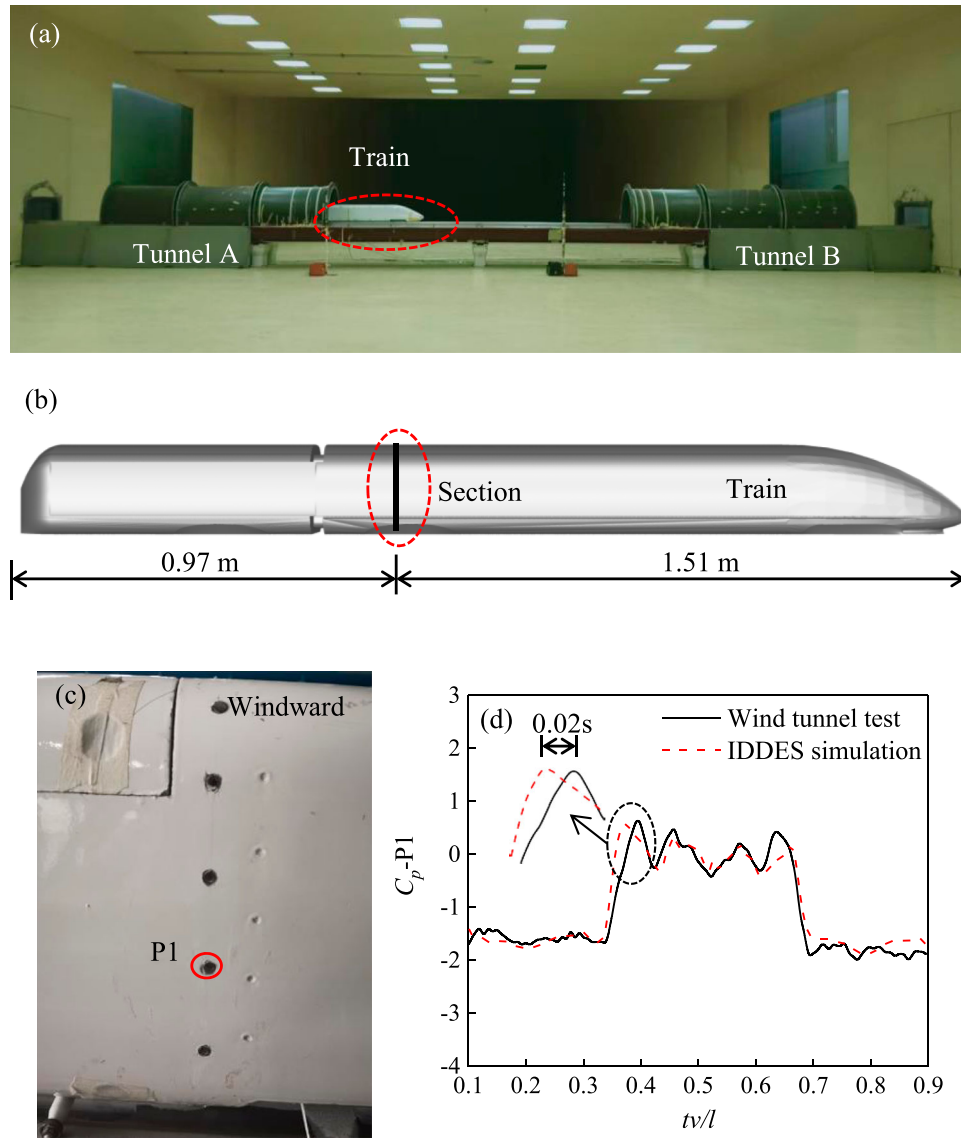
Figure 7. Verification of wind tunnel test: (a) Schematic of the wind tunnel laboratory of Central South University; (b) train model; (c) location of measuring point; (d) time-history curve of measuring point P1.

medium mesh can save computing resources whilst keeping the calculation error between the fine and medium meshes. Therefore, the medium mesh is chosen as the mesh generation scheme of the numerical model in this study.

2.3.2. Comparison with the results of wind tunnel moving model test

To verify the reliability of the numerical method presented in this study, a corresponding CFD model was established by referring to the moving train model test device with a scale of 1:16.8 in the wind tunnel laboratory of Central South University, China. The grid scheme of the train boundary layer of the CFD model is consistent with that in Figure 4. The incoming crosswind velocity and the train speed are 8 and 6 m/s, respectively. The train

runs on the leeward side line, and the measuring point P1 is located on the windward side of the train. v and l represent the train speed and width of the wind tunnel, respectively. Figure 7 shows the comparison between the numerical model and the time-history curve of the train measuring point pressure coefficient in the wind tunnel test. The time-history curve of the pressure coefficient of the measuring point obtained based on the IDDES turbulent model is in good agreement with the wind tunnel test results in terms of numerical value and curve fluctuation law. When the train leaves tunnel A, the pressure coefficient curve in the numerical model rises faster than the test curve, and the time difference for the pressure coefficient at the measuring point to reach the peak value is 0.02 s. This finding is mainly because when the train enters tunnel A, its speed will be disturbed and will be
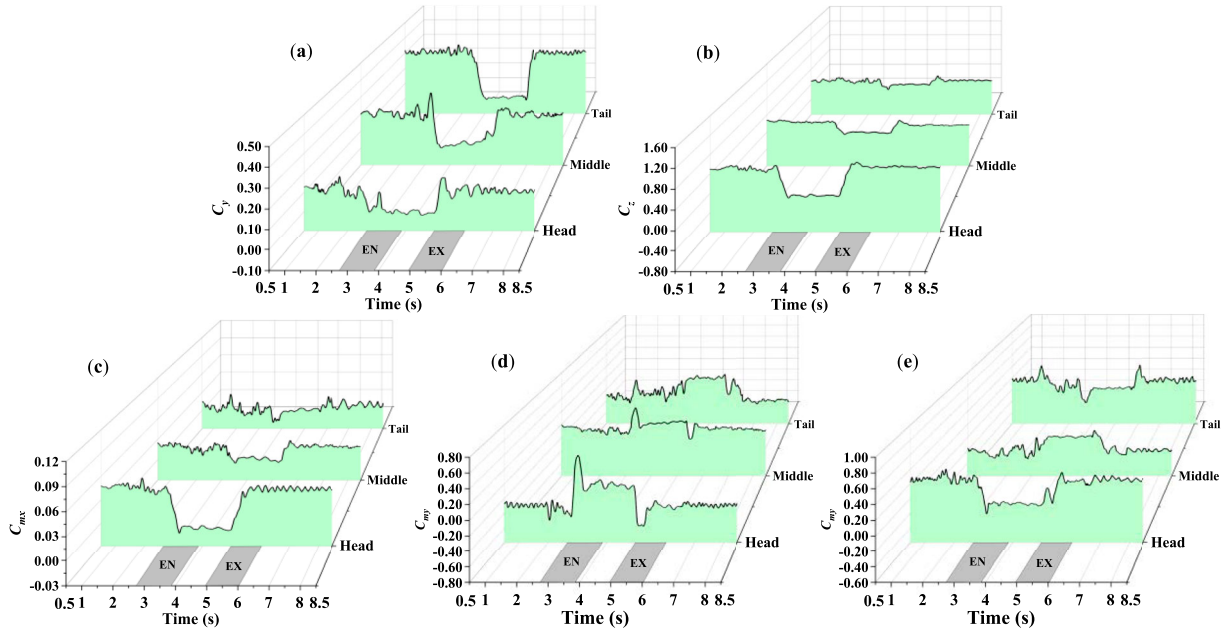
Figure 8. Time-history curves of aerodynamic load coefficient of the three carriages corresponding to BL: (a) lift force, (b) side fore, (c) rolling moment, (d) yawing moment and (e) pitching moment.

slightly lower than the speed of the numerical model due to the limitation of the test conditions. Other subtle differences in the curve may be affected by the following conditions: (1) The train speed is constant in the numerical model, whereas the train speed in the wind tunnel test is disturbed by many factors, such as wheel rail friction. (2) In the test, the bottom of the train is closely connected with the track, and the distance between the bottom of the train and the bridge deck in the numerical model is about 1 cm. Therefore, the parameters of the IDDES turbulence model are suitable in this study, and the calculation results are reliable.

3. Results and analysis

3.1. Buffering effect analysis

3.1.1. Aerodynamic load coefficient

Figure 8 shows the time-history of aerodynamic load coefficient of the HST in the whole process of running through the noise barrier under 30 m/s crosswind condition corresponding to the BL case. The train running speed is 250 km/h. In the figure, 'EN' represents the time period (2.75–3.85 s) between the time when the nose tip of the head carriage reaches the noise barrier to the time when the noise tip of the tail carriage enters the noise barrier. 'EX' represents the time period (4.95–6.05 s) between the time when the nose tip of the head carriage exits the noise barrier to the time when the noise tip of the tail carriage exits the noise barrier. In accordance with the analysis from Figure 8, the aerodynamic loads of the three

carriages in the processes of 'EN' and 'EX' show dramatic changes, which indicates that the running safety of train is reduced remarkably. Except for the aerodynamic lift force, the amplitude values ($\Delta C = C_{\max} - C_{\min}$) of the remaining four aerodynamic loads during 'EN' and 'EX' processes are all the highest for the head carriage, which is 2–3 times of the corresponding values of the middle and tail carriages. Considering that the contribution of aerodynamic lift amplitude to running safety deterioration is relatively weak, the head carriage can be used as the target carriage to test the buffering effect of the two types of structures. The aerodynamic load amplitudes of the head carriage in the 'EN' process are comparable to the corresponding values in the 'EX' process, and the former is slightly higher than the latter (Figures 8(d) and (e)).

Figure 9 shows the comparison of the aerodynamic load time-history curves of the head carriage when entering the noise barrier under the condition that the two types of buffer structures take different lengths. From the perspective of aerodynamic load, the reduction rate of aerodynamic load amplitude ($\Delta = [(\Delta C_{buffer} - \Delta C_{BL})/\Delta C_{BL}] \times 100\%$) is used to quantitatively reflect the buffering effect, and the specific value is shown in Table 1.

On the basis of the analysis in Figure 9 and Table 1, the two types of buffer structures have a certain buffering effect on the sudden amplitude of aerodynamic load on the whole. For the TRI, the amplitudes of aerodynamic lift and side forces and rolling moment are abnormally increased after the buffer structure is installed. For example, the installation length of 2 L TRI can lead to an
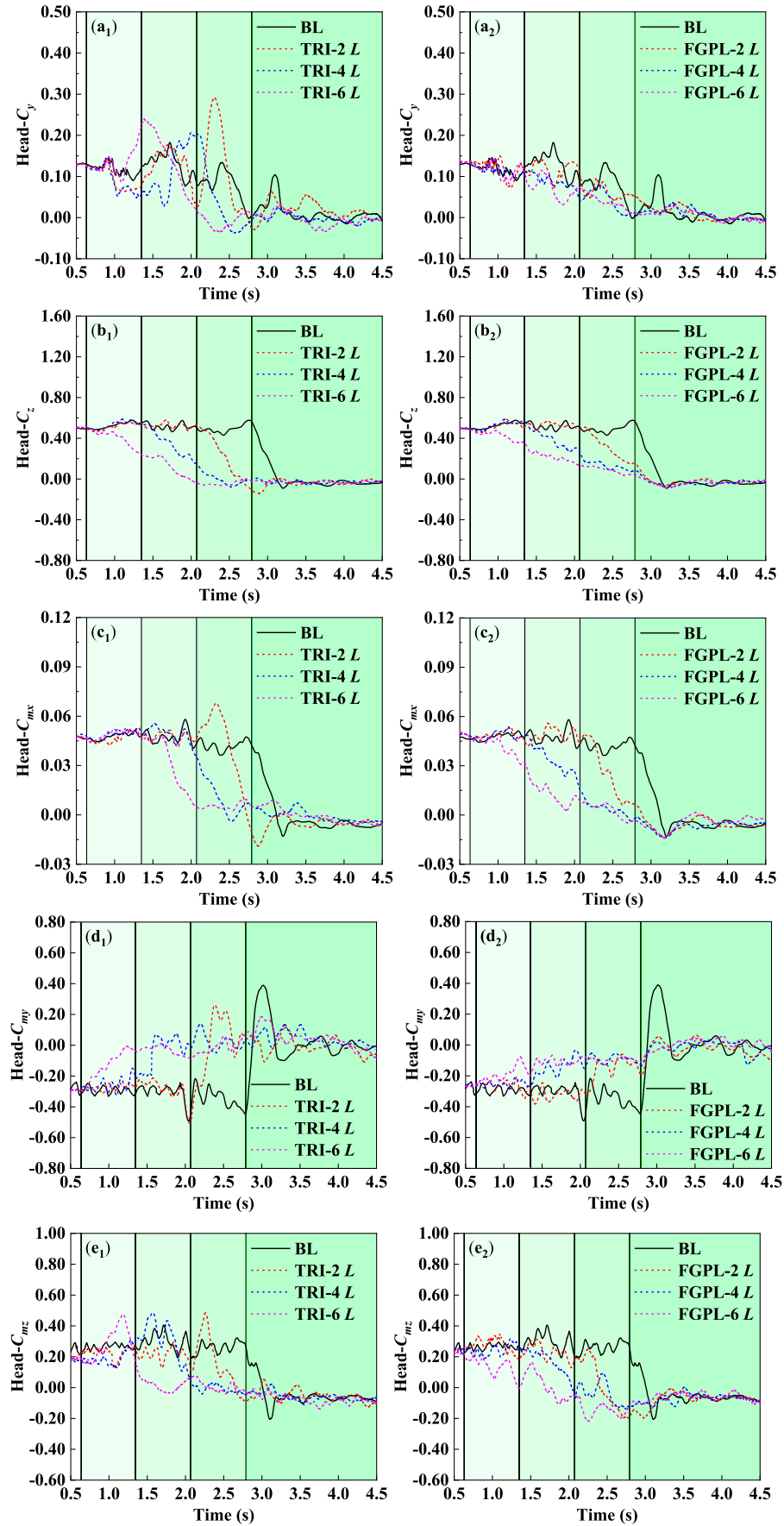
Figure 9. Time-history curve of the aerodynamic load coefficient of the head carriage when entering the noise barrier under two types of buffer structures: (a1)–(e1) triangle type; (a2)–(e2) fence type.

Table 1. Reduction rate of the aerodynamic load amplitude under two types of buffer structures.

Coefficient	BL $\mid\Delta C\mid$max	TRI-2 L Δ_1	TRI-4 L Δ_2	TRI-6 L Δ_3	FGPL-2 L Δ_4	FGPL-4 L Δ_5	FGPL-6 L Δ_6
C_y	0.18	−73.5%	−31.9%	−48.1%	24.8%	28.0%	26.3%
C_z	0.67	−8.7%	0.6%	13.8%	0.4%	1.2%	12.0%
C_{mx}	0.07	−22.5%	15.5%	16.9%	1.6%	4.8%	9.7%
C_{my}	0.88	12.8%	47.2%	45.7%	50.3%	65.2%	67.6%
C_{mz}	0.61	0.3%	2.3%	0.2%	10.4%	25.1%	25.1%

inverse increase of 73.5% in the lift amplitude. With the increase in the buffer length, the buffering effect of TRI appears gradually. The buffering effect when the length of TRI is 6 L is less different from that when it is 4 L, which indicates that the buffering effect tends to be stable after the length of TRI increases to 4 L. However, TRI still causes the aerodynamic loads to drop in a step-like manner, such as the rolling and pitching moments (Figures 9 (c_1) and (e_1)). FGPL shows a certain buffering effect under different length conditions. Compared with TRI, FGPL can make the aerodynamic load change process smoother, especially the buffering effect on the amplitudes of aerodynamic lift, yawing and pitching moments. For example, the reduction rate of the above three indexes can reach 26.3%, 67.6% and 25.1% when the FGPL length reaches 6 L, respectively. However, the buffering effect levels off when its length reaches 4 L.

3.1.2. Dynamic responses

Figures 10(a) and (b) show the vertical and lateral acceleration time-history curves of the head carriage when entering the noise barrier under the condition that the two types of buffer structures take different lengths, respectively. Figure 10(c) shows the quantitative relation between peak lateral acceleration and corresponding buffer length.

As shown in Figure 10(a), the vertical acceleration of the carriage presents the characteristics of wavy low-frequency fluctuation. This condition is mainly caused by the vibration of the carriage under the action of the suspension system when the carriage body is excited by the sudden aerodynamic lift force. The vibration frequency depends on the natural frequency of the carriage body. The lateral acceleration of a carriage is an important index of running safety. The vertical acceleration amplitude in TRI is higher than that in BL, and the corresponding amplitude in the FGPL is lower than that in the BL. This finding further reveals the safety hazards of the TRI scheme. Compared with the vertical acceleration, the lateral acceleration can better reflect the train running safety and passenger comfort. As shown in Figures 10(b) and (c), the peak lateral acceleration decreases monotonically with the length of the buffer section (TRI or FGPL). When the buffer length increases from 0 L to 6

L, the peak lateral acceleration for TRI decreases by only 55%. The peak lateral acceleration for FPGL is reduced by 62%. The buffering effect of FGPL is still better than that of TRI from the perspective of lateral acceleration.

The derailment coefficient of carriage wheelset can directly reflect the train running safety. Figures 11 (a)–(d) show the time-history curves of derailment coefficient of the four wheelsets of the head carriage when entering the noise barrier under the condition that the two types of buffer structures take different lengths, respectively. Figure 11(e) shows the quantitative relation between the peak derailment coefficient (including the corresponding wheel position) and corresponding buffer length. In the figure, WWS and LWS represent the windward and leeward sides, respectively.

As shown in Figure 11, the high amplitude fluctuation of derailment coefficient appears in the four leeward wheels, especially in the second and fourth wheels. The reason for this phenomenon is that when the carriage is affected by the crosswind, the whole carriage is inclined to the leeward side, and the leeward side wheel tread is in close contact with the rail top surface. For the BL, the derailment coefficient of the windward side four wheels has a slight upward trend when the head carriage enters the noise barrier; the leeward side wheels suddenly exhibit high amplitude immediately. This condition is due to the sudden unloading of the aerodynamic load, and the windward side wheel has transient impact with the rail top surface during the falling process. From the quantitative point of view (Figure 11(e)), the peak derailment coefficient of the train exceeds the corresponding safety limit (Deng et al., 2019) under the condition that the noise barrier is not installed with the buffer structure. For the TRI, the peak derailment coefficient increases to 0.85 when the buffer length is 2 L. whereas it decreases by 33% when the buffer length is increased to 6 L compared with the BL. For the FGPL, the peak derailment coefficient decreases by 33% when the buffer length only increases to 4 L, and the decrease is no longer remarkable with the continuous increase in the length compared with the BL. In conclusion, the buffering effect of FGPL is superior to TRI, and the buffer length of 4 L is the most reasonable (considering the construction cost).
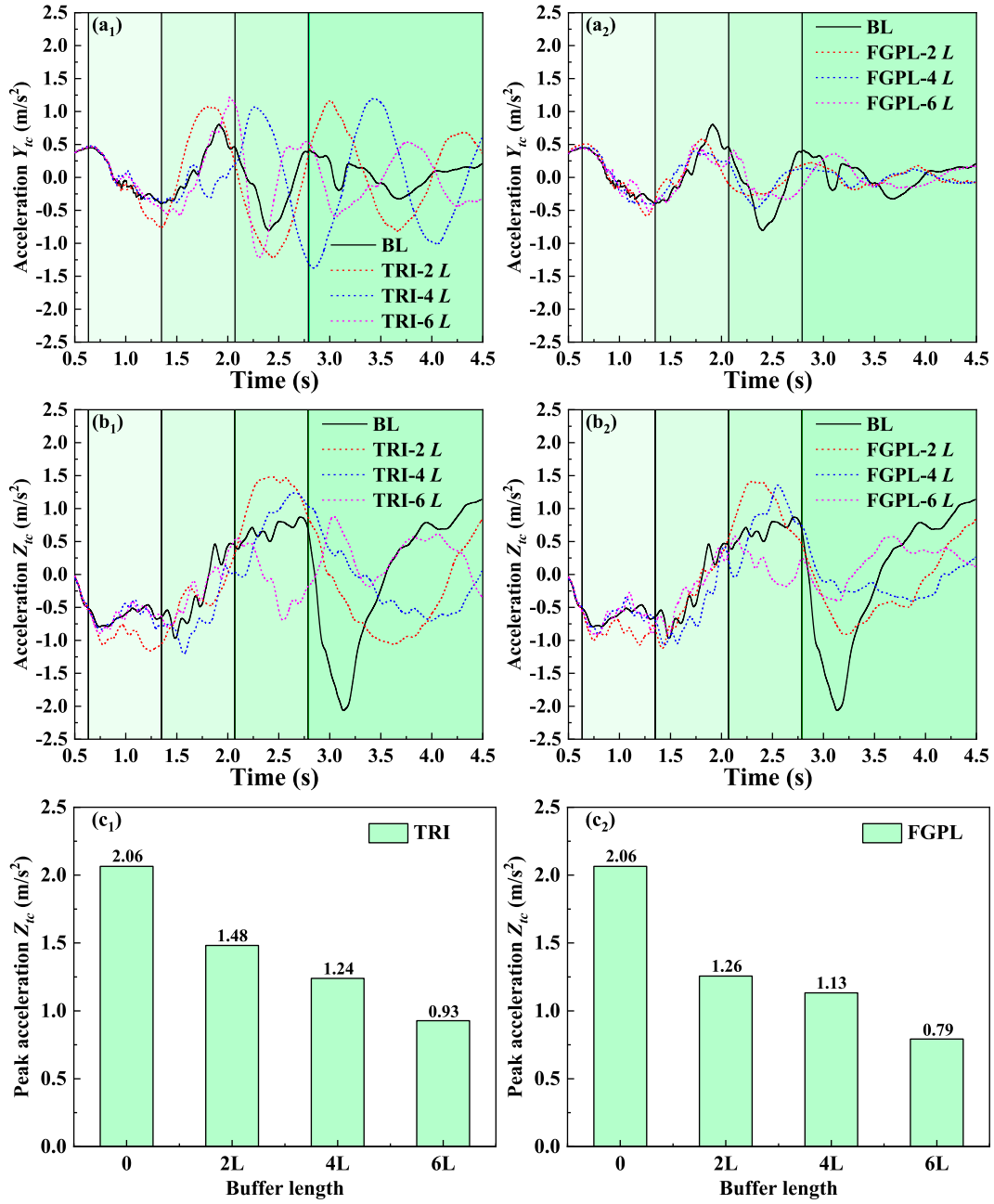
Figure 10. Acceleration of the head carriage when entering the noise barrier under two types of buffer structures: (a) vertical acceleration time-history; (b) lateral acceleration time-history; and (c) peak value.

3.2. Buffer mechanism

3.2.1. Distribution of wind velocity

The longitudinal distribution gradient of the Z-component wind velocity on the train running line is the main factor affecting the sudden change amplitude of the train aerodynamic loads. Figure 12 shows the mean value distribution of Z-component wind velocity on the longitudinal profile of the windward line centre (Figure 12 (a)) under each case before the train arrives at the noise barrier (or buffer section). The sample for calculating the mean value is taken from the data of 100 consecutive

time steps; the wind velocity value is dimensionless by dividing the value of incoming flow velocity (U_{if}).

In accordance with the analysis in Figure 12, the wind velocity distribution law is the same in the longitudinal area except the buffer section, namely, the open line area and the leeward area of the noise barrier. This condition shows that the setting of the buffer section has no effect on the wind velocity distribution in the longitudinal area outside the buffer section. The wind velocity in the open line area is in the positive direction, which is consistent with the incoming flow. The wind velocity
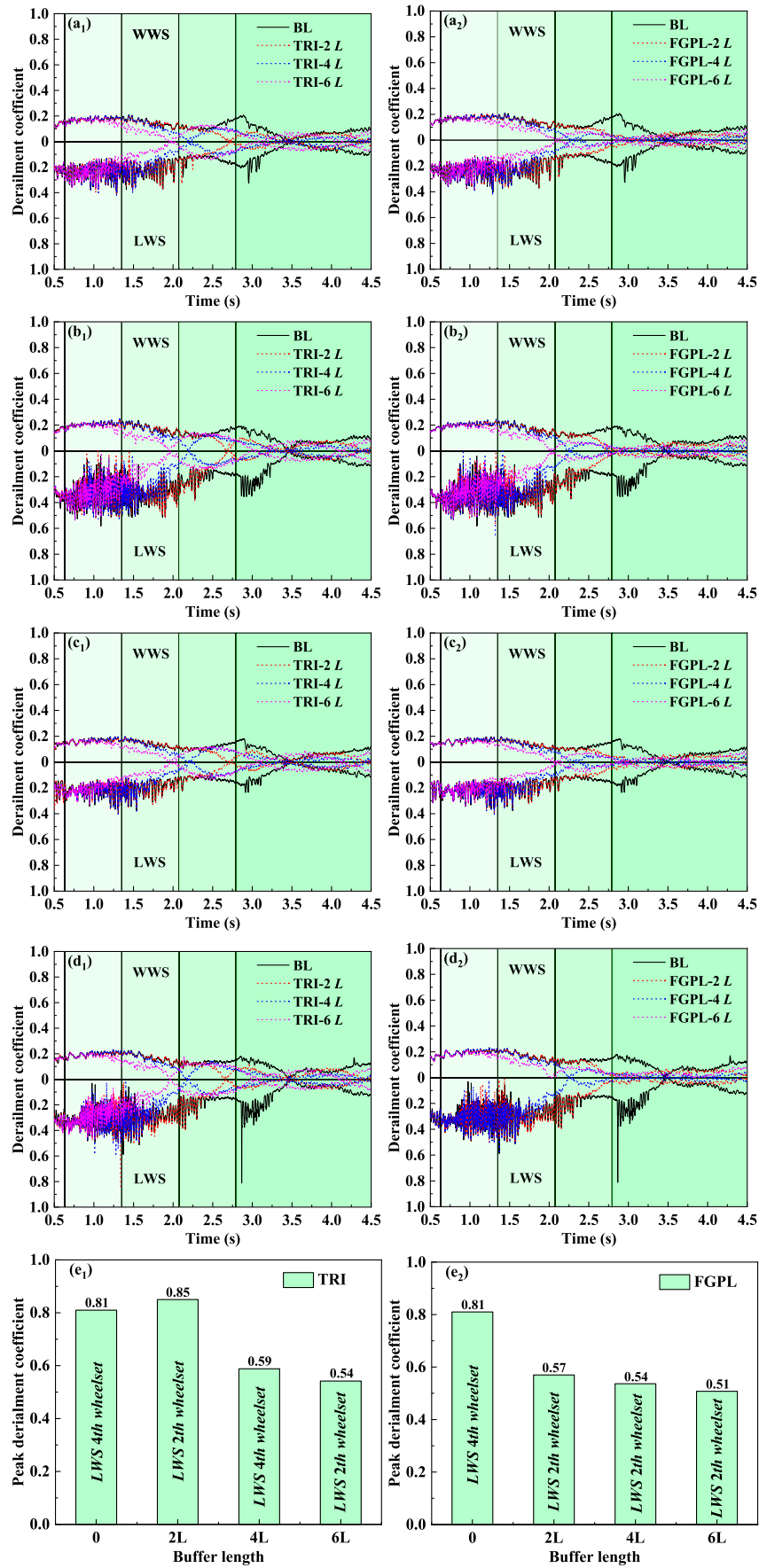
Figure 11. Derailment coefficient of the head carriage when entering the noise barrier under two types of buffer structures: (a) first wheelset; (b) second wheelset; (c) third wheelset; (d) fourth wheelset; and (e) peak value.
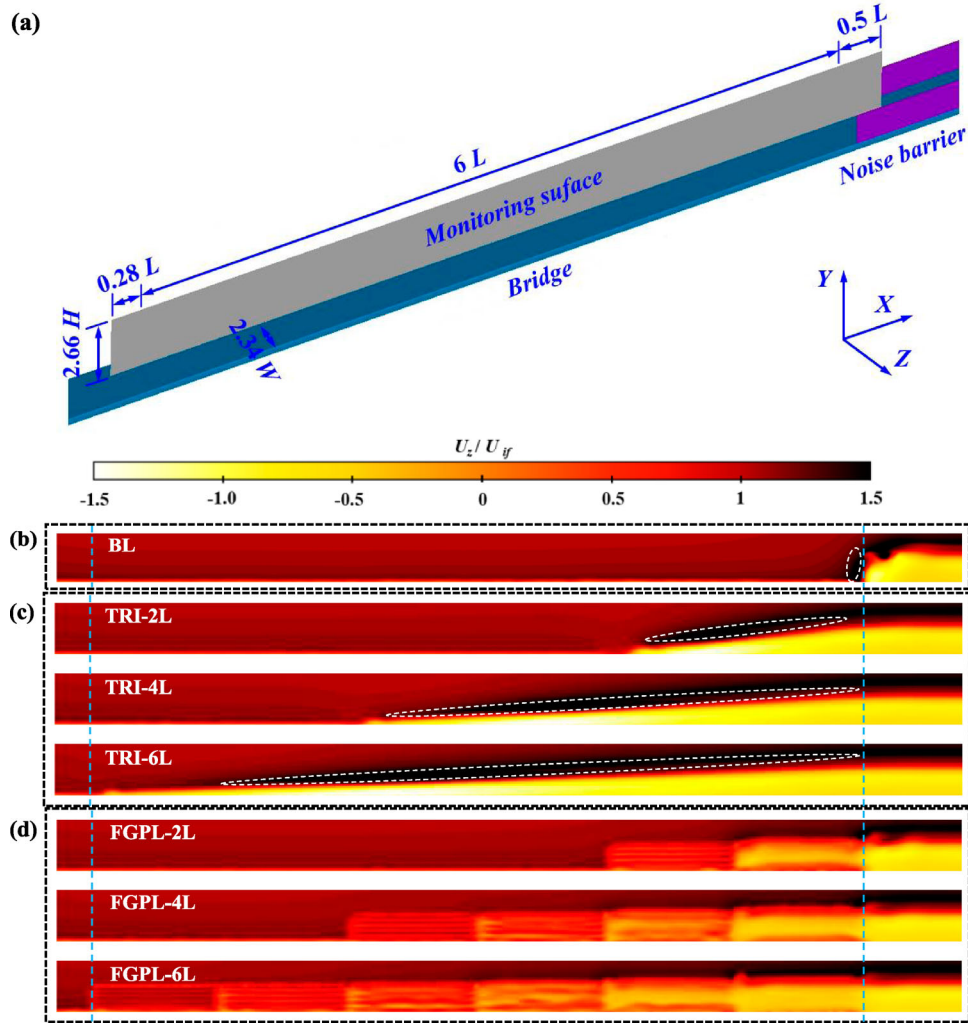
Figure 12. Distribution of wind speed on the centre longitudinal profile of windward line: (a) location of monitoring surface (b) BL; (c) TRI; and (d) FGPL.

in the leeward area of the noise barrier is close to zero, and reverse wind appears. This condition may be caused by the vortex formed on the leeward side of the noise barrier after the incoming flow bypasses the top of the noise barrier. For the BL, the cliff-like abrupt area of the wind velocity distribution appears at the vertical end of the noise barrier. This area is bounded by the vertical end of the noise barrier, the outside is the acceleration area of wind velocity (the dimensionless value is up to 1.5), and the inside is the negative direction area. The existence of the cliff-like abrupt area is the fundamental reason for the sudden change in train aerodynamic load. For the TRI, the wind abrupt area is distributed along the upper edge of the triangle. The slope of the abrupt area boundary of the abrupt area decreases with the length of the triangle, resulting in a buffering effect. However, the dimensionless wind velocity value of the acceleration area on the upper edge still reaches 1.5, which indicates that the buffering effect of triangle type is potentially

problematic. For the FGPL, the wind velocity gradient from outside to inside in the longitudinal direction is smooth and decreases gently with the decrease in porosity. The vertical distribution of the wind velocity in the buffer zone is uniform because the height of each unit plane remains the same. The longer the fence, the flatter the gradient of wind velocity along the longitudinal direction. No remarkable abrupt area is observed in wind velocity along the upper edge of the fence. Thus, the buffer effect of the fence type is better than that of the triangle type on the whole.

3.2.2. Transient streamline structure

Figure 13 shows the schematic of the four typical positions #1, #2, #3 and #4 when the train enters the noise barrier. Figure 14 shows the evolution process of streamline structures on the middle cross sectional slice of the three carriages when the train enters the noise barrier (corresponding to the four positions in Figure 13) under
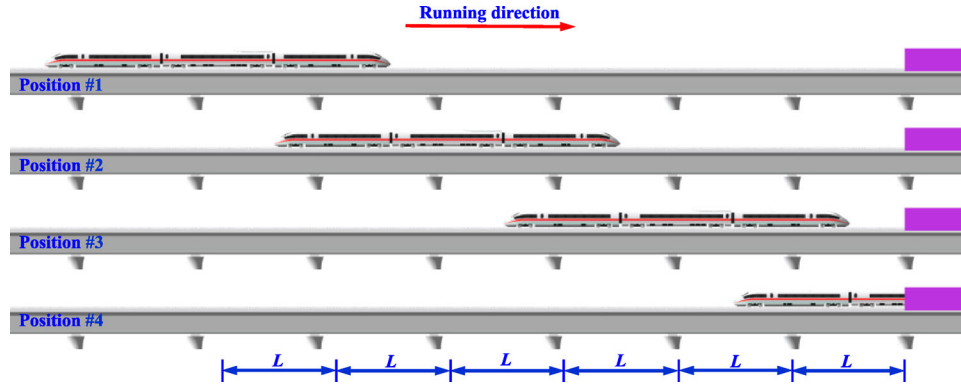
Figure 13. Schematic of the train position.

the condition that the two types of buffer structures take different lengths.

As shown in Figure 14, the high-velocity area is mainly distributed on the top of the carriage, and the highest velocity can reach twice the incoming flow velocity. For the BL (Figure 14(a)), a large number of chaotic small vortex structures appeared around the carriage body that has entered the noise barrier due to the blocking effect of the solid noise barrier. The flow speed of the corresponding area is remarkably reduced (position #4), which is in sharp contrast to the area around the carriage body which is still on the open line, thereby causing the sudden change in the aerodynamic load of the train.

For the TRI, an obvious high velocity area is still observed on the carriage top when the head carriage enters the triangular buffer section, as shown in Figures 14(b) position #3, (c) position #2 and (d) position #2. This phenomenon is because the height of the triangle at the corresponding position has not reached the extent of completely covering the height of the carriage, and the crosswind flow forms a new accelerated flow around the carriage top after bypassing the triangle top. The high-velocity area disappears immediately at the corresponding immediate next position. Thus, the fluctuation amplitude of train aerodynamic load in different triangle lengths still exhibits the phenomenon of inverse increase.

For the FGPL, the flow velocity decreases to different degrees (the decreasing amplitude is negatively correlated with the porosity) after the streamlines pass through the pores of the fence, and this decrease is uniform in the vertical direction. This finding is consistent with the phenomenon revealed in Figure 12(d), showing that the rectangular fence has a good energy dissipation effect on incoming flow. As shown in Figures 14(f) and (g), the flow structure around the carriage body has good consistency in the longitudinal direction when the carriage is completely driven into the fence section and has low flow velocity. This condition shows that the fence on the leeward side has a good pressure relief effect on the flow field

with high vorticity on the leeward side of the carriage body. Thus, the FGPL can achieve a smooth transition of train flow field from full-crosswind mode to solid noise barrier mode, and sufficient effect can be obtained when the buffer length reaches 4 L.

3.2.3. Pressure distribution on the carriage surface

The pressure distribution on the carriage body surface directly determines the intensity of aerodynamic load variation. Figure 15 shows the cloud diagram of the pressure distribution on the carriage body surface corresponding to the typical positions in Figure 13 under various cases. The following findings are obtained from Figure 15.

For the BL, the windward side of the carriage body exposed to the crosswind is subjected to a strong positive pressure (Figure 15(a)), and the pressure on the carriage body surface inside the noise barrier is approximately zero. The vertical boundary of the end of the noise barrier corresponds to the boundary of the pressure abrupt area, which is consistent with the wind velocity distribution law revealed in Figure 12(a). The huge difference in the pressure distribution on the carriage surface along the longitudinal direction leads to the sudden change in aerodynamic load.

For the TRI (Figure 15(b)), a remarkable pressure abrupt area is still observed on the windward surface of the carriage body, and the abrupt boundary line corresponds to the top edge of the triangle. The longer the triangle, the smaller the slope of the abrupt boundary. The presence of the slanted pressure abrupt boundary line on the carriage windward surface makes the rolling moment amplitude of the carriage reverse rise when it enters the buffer section (Figure 9(c_1)). This condition is the root cause of the safety hazard of the TRI buffer scheme. For the FGPL (Figure 15(c)), the pressure distribution on the windward side surface of the train body is uniform along the vertical direction. Only a weak pressure gradient is observed in the longitudinal direction
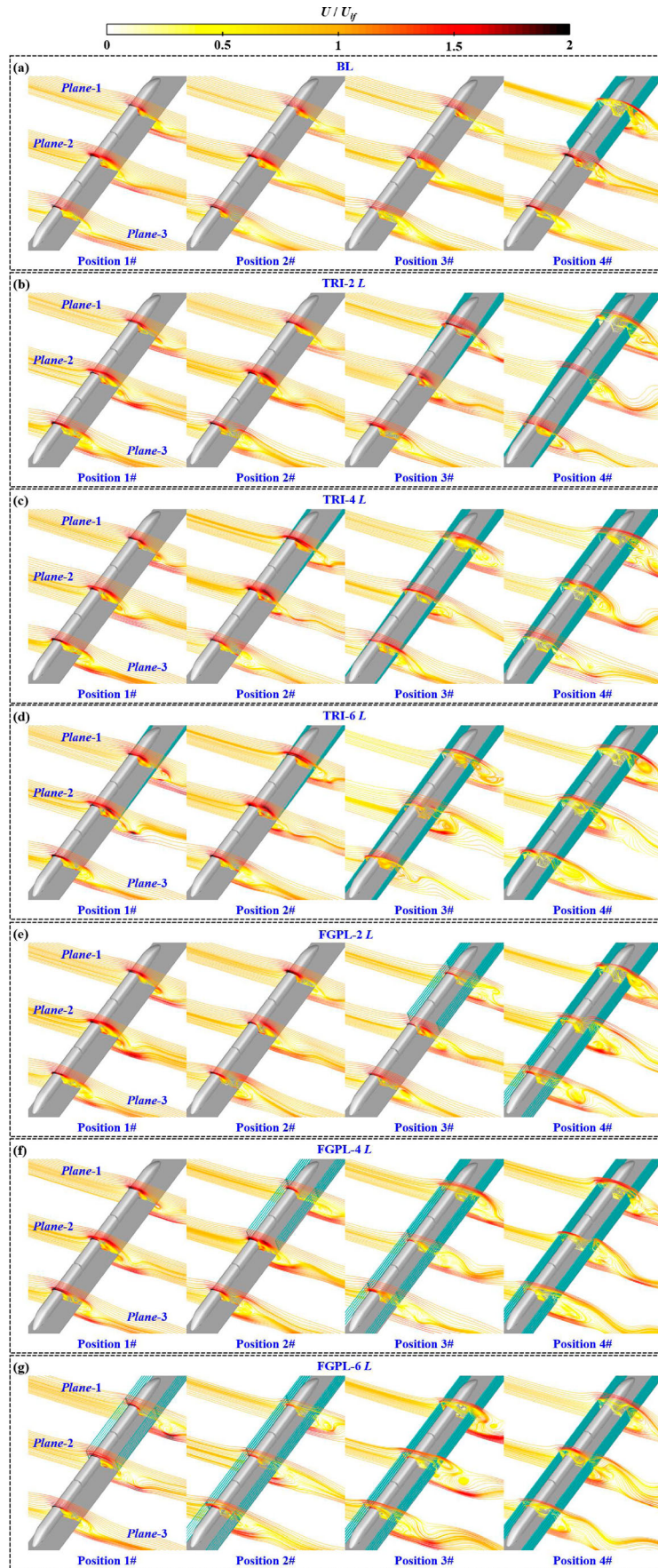
Figure 14. Streamline structures on the middle cross sectional slice of the three carriages when the train enters the noise barrier: (a) BL; (b)– (d) TRI; and (e)–(g) FGPL.
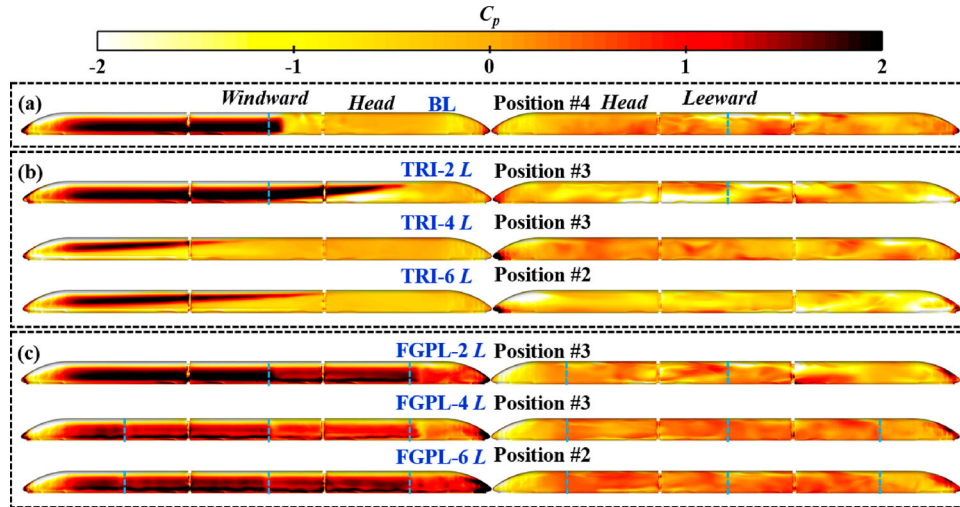
Figure 15. Pressure distribution on the train surface: (a) BL; (b) TRI; and (c) FGPL.

when the buffer length reaches 4 L, which is caused by the gradual change in porosity along the longitudinal direction. Weak pressure gradient is a strong guarantee for small aerodynamic load fluctuation amplitude. This phenomenon confirms that the FGPL-4 L scheme has an excellent buffering effect.

4. Conclusions and future perspectives

Two types of aerodynamic buffer structures (triangle and fence) installed at the end of the noise barrier are compared comprehensively based on IDDES and vehicle multi-body dynamics to address the aerodynamic performance deterioration of trains passing through the end of the bilateral vertical noise barrier under crosswinds. The optimal scheme and parameters are obtained. The main conclusions are as follows.

(1) The head carriage can be used as the target carriage to test the buffering effect of the two types of structures. The aerodynamic load amplitudes of the HST when entering the noise barrier are comparable to the corresponding values when exiting, and the former is slightly higher than the latter.
(2) From the perspective of aerodynamic load, the buffering effect of FGPL is better than that of TRI. The installation length of 2 L TRI can lead to an inverse increase of 73.5% in the lift amplitude. Compared with the TRI, the FGPL can make the aerodynamic load change process smoother.
(3) From the perspective of dynamic response, the buffering effect of FGPL is superior to TRI, and the buffer length of 4 L is the most reasonable. For the TRI, the peak derailment coefficient increases to 0.85 when the buffer length is 2 L compared

with the BL. For the FGPL, the peak derailment coefficient decreases by 33% when the buffer length only increases to 4 L, and the decrease is no longer remarkable with the continuous increase in length compared with the BL.
(4) From the perspective of dynamic response, the presence of the slanted pressure abrupt boundary line on the carriage windward surface makes the rolling moment amplitude of the carriage reverse rise when it enters the TRI buffer section; whereas the FGPL can achieve a smooth transition of train flow field from full-crosswind mode to solid noise barrier mode.

However, only single wind velocity and train speed conditions were considered in this study. The performance of the buffer structure may behave differently when the aforementioned conditions change. Therefore, a more systematic and comprehensive study on train running safety assessment based on the proposed buffer scheme is needed in the subsequent work, such as wind tunnel moving model test.

Disclosure statement

Funding

References

BS EN. (2006). Railway applications - aerodynamics-Part5: requirements and test procedures for aerodynamics in tunnels. BS EN 14067-5, 7-9.

Chen, F., Peng, H. R., Ma, X. X., Liang, J. Y., Hao, W., & Pan, X. D. (2019). Examining the safety of trucks under crosswind at bridge-tunnel section: A driving simulator study. *Tunnelling and Underground Space Technology*, *92*, 103034. https://doi.org/10.1016/j.tust.2019.103034

Chen, Z. W., Liu, T. H., Guo, Z. J., Huo, X. S., Li, W. H., & Xia, Y. T. (2022). Dynamic behaviors and mitigation measures of a train passing through windbreak transitions from ground to cutting. *Journal of Central South University*, *29*(8), 2675–2689. https://doi.org/10.1007/s11771-022-5114-6

Deng, E., Yang, W. C., Lei, M. F., Zhu, Z. H., & Zhang, P. P. (2019). Aerodynamic loads and traffic safety of high-speed trains when passing through two windproof facilities under crosswind: A comparative study. *Engineering Structures*, *188*, 320–339. https://doi.org/10.1016/j.engstruct.2019.01.080

Dong, T. Y., Minelli, G., Wang, J. B., Liang, X. F., & Krajnovic, S. (2022). Numerical investigation of a high-speed train underbody flows: Studying flow structures through large-eddy simulation and assessment of steady and unsteady Reynolds-averaged Navier-Stokes and improved delayed detached eddy simulation performance. *Physics of Fluids*, *34*(1), 015126. https://doi.org/10.1063/5.0075617

Gao, H. R., Liu, T. H., Gu, H. Y., Jiang, Z. W., Huo, X. S., Xia, Y. T., & Chen, Z. W. (2021). Full-scale tests of unsteady aerodynamic loads and pressure distribution on fast trains in crosswinds. *Measurement*, *186*, 110152. https://doi.org/10.1016/j.measurement.2021.110152

He, J. J., Xiang, H. Y., Li, Y. L., & Han, B. (2022). Aerodynamic performance of traveling road vehicles on a single-level rail-cum-road bridge under crosswind and aerodynamic impact of traveling trains. *Engineering Applications of Computational Fluid Mechanics*, *16*(1), 335–358. https://doi.org/10.1080/19942060.2021.2012516

Jing, H. Q., Ji, X. Y., He, X. H., Zhang, S. F., Zhou, J. C., & Zhang, H. Y. (2022). Dynamic characteristics of unsteady aerodynamic pressure on an enclosed housing for sound emission alleviation caused by a passing high-speed train. *Applied Sciences*, *12*(3), 1545. https://doi.org/10.3390/app12031545

Kim, D. H., Cheol, S. Y., Iyer, R. S., & Kim, H. D. (2021). A newly designed entrance hood to reduce the micro pressure wave emitted from the exit of high-speed railway tunnel. *Tunnelling and Underground Space Technology*, *108*, 103728. https://doi.org/10.1016/j.tust.2020.103728

Li, T., Dai, Z. Y., Yu, M. G., & Zhang, W. H. (2021). Numerical investigation on the aerodynamic resistances of double-unit trains with different gap lengths. *Engineering Applications of Computational Fluid Mechanics*, *15*(1), 549–560. https://doi.org/10.1080/19942060.2021.189532119942060.2021.1895321

Li, T., Qin, D., Zhou, N., & Zhang, W. H. (2022). Step-by-step numerical prediction of aerodynamic noise generated by high speed trains. *Chinese Journal of Mechanical Engineering*, *35*(1), 28. https://doi.org/10.1186/s10033-022-00705-4

Liao, H., Sun, Y., Li, T., & Zhang, J. (2023). Influence of marshalling length on aerodynamic characteristics of urban emus under crosswind. *Journal of Applied Fluid Mechanics*, *16*(1), 9–20. https://doi.org/10.47176/JAFM.16.01.1338

Liu, T. H., Chen, Z. W., Zhou, X. S., & Zhang, J. (2018). A CFD analysis of the aerodynamics of a high-speed train passing through a windbreak transition under crosswind. *Engineering Applications of Computational Fluid Mechanics*, *12*(1), 137–151. https://doi.org/10.1080/19942060.2017.1360211

Miyachi, T., & Fukuda, T. (2021). Model experiments on area optimization of multiple openings of tunnel hoods to reduce micro-pressure waves. *Tunnelling and Underground Space Technology*, *115*, 103996. https://doi.org/10.1016/j.tust.2021.103996

Qiu, X. W., Li, X. Z., Zheng, J., & Wang, M. (2022). Fluctuating wind pressure on vertical sound barrier during two high-speed trains passing each other. *International Journal of Rail Transportation*, *10*, 1–18. https://doi.org/10.1080/23248378.2022.2062062

Soper, D., Gillmeier, S., Baker, C., Morgan, T., & Vojnovic, L. (2019). Aerodynamic forces on railway acoustic barriers. *Journal of Wind Engineering and Industrial Aerodynamics*, *191*, 266–278. https://doi.org/10.1016/j.jweia.2019.06.009

TB/T 3352-2014. (2014). PSD of ballastless track irregularity of high-speed Railway. (in Chinese).

Wang, T. T., Zhu, Y., Tian, X. D., Shi, F. C., Zhang, L., & Lu, Y. B. (2022). Design method of the variable cross-section tunnel focused on improving passenger pressure comfort of trains intersecting in the tunnel. *Building and Environment*, *221*, 109336. https://doi.org/10.1016/j.buildenv.2022.109336

Wang, Y. P., Zhang, Z. Y., Zhang, Q. W., Zhen, H., & Su, C. Q. (2021). Dynamic coupling analysis of the aerodynamic performance of a sedan passing by the bridge pylon in a crosswind. *Applied Mathematical Modelling*, *89*, 1279–1293. https://doi.org/10.1016/j.apm.2020.07.003

Winslow, A., & Howe, M. S. (2005). Stepwise approximation of an optimally flared tunnel portal. *Journal of Sound and Vibration*, *280*(3-5), 983–995. https://doi.org/10.1016/j.jsv.2004.01.039

Xiong, X. H., Yang, B., Wang, K. W., Liu, T. H., He, Z., & Zhu, L. (2020). Full-scale experiment of transient aerodynamic pressures acting on a bridge noise barrier induced by the passage of high-speed trains operating at 380–420 km/h. *Journal of Wind Engineering and Industrial Aerodynamics*, *204*, 1042980. https://doi.org/10.1016/j.jweia.2020.104298

Yang, W. C., Deng, E., Lei, M. F., Zhu, Z. H., & Zhang, P. P. (2019). Transient aerodynamic performance of high-speed trains when passing through two windproof facilities under crosswinds: A comparative study. *Engineering Structures*, *188*, 729–744. https://doi.org/10.1016/j.engstruct.2019.03.070

Zhang, L., Thurow, K., Stoll, N., & Liu, H. (2018). Influence of the geometry of equal-transect oblique tunnel portal on compression wave and micro-pressure wave generated by high-speed trains entering tunnels. *Journal of Wind Engineering and Industrial Aerodynamics*, *178*, 1–17. https://doi.org/10.1016/j.jweia.2018.05.003

Zhang, Q. W., Su, C. Q., & Wang, Y. P. (2020). Numerical investigation on aerodynamic performance and stability of a sedan under wind-bridge-tunnel road condition. *Alexandria Engineering Journal*, *59*(5), 3963–3980. https://doi.org/10.1016/j.aej.2020.07.004

Zhang, T., Xia, H., & Guo, W. W. (2018). Analysis on running safety of train on the bridge considering sudden change of wind load caused by wind barriers. *Frontiers of Structural and Civil Engineering, 12*(4), 558–567. https://doi.org/10.1007/s11709-017-0455-1

Zheng, J., Li, X. Z., Qiu, X. W., Liu, D. J., Zhao, S. H., & Qian, Y. L. (2022). Field study on train-induced aerodynamic pressure near the entrance of fully enclosed sound barriers. *Vehicle System Dynamics*, 1–18. https://doi.org/10.1080/00423114.2022.2071746

Zhou, L., Liu, T. H., Chen, Z. W., Li, W. H., Guo, Z. J., He, X. H., & Wang, Y. W. (2021). Comparison study of the effect of bridge-tunnel transition on train aerodynamic performance with or without crosswind. *Wind and Structures, 32*(6), 597–612. https://doi.org/10.12989/was.2021.32.6.597